MODELING OF DOWNSTREAM HEATING IN MELT ELECTROSPINNING OF POLYMERS

A Thesis

by

NIKHIL MAYADEO

Submitted to the Office of Graduate and Professional Studies of
Texas A&M University
in partial fulfillment of the requirements for the degree of

MASTER OF SCIENCE

Chair of Committee,	Micah Green
Committee Members,	Mohammad Naraghi
	Yossef Elabd
Head of Department,	M. Nazmul Karim

August 2017

Major Subject: Chemical Engineering

ABSTRACT

The current study is driven by the demand for sub-micron fibers with high surface area to volume ratios to be used in applications such as high performance filtration, tissue engineering, in-situ wound dressing, drug delivery, thermal management, and energy storage.

Traditionally, industry has been using solution electrospinning for manufacturing sub-micron fibers. However, it is expensive and environmentally unfavorable because a significant quantity of toxic solvent is lost to the surroundings during this process. The alternative approach, melt electrospinning, is inherently limited to the production of micron-sized fibers. This is mainly due to the high viscosity and low electrical conductivity of the melt. In addition, rapid heat loss to the surroundings results in solidification of the polymer melt jet before it has been significantly stretched by the electric field.

In order to address this problem, we propose that a volumetric heat source placed downstream in the melt electrospinning process can lead to markedly decreased fiber diameters. For this purpose, we utilize a model for non-isothermal melt electrospinning in the presence of a downstream volumetric heat source. The model is based on thin filament approximation applied to fully coupled momentum, continuity, charge, and energy equations, along with the non-isothermal Giesekus constitutive model and the electric field equation at steady state.

The simulation results demonstrate that downstream heating does reduce the fiber diameter, and is therefore a feasible solution for resolving the drawbacks of melt electrospinning. In addition, the model has been used to capture the influence of the surrounding temperature, which affects the thinning of the fiber through surface rather than volumetric interactions. Finally, experiments on melt electrospun polycaprolactone are utilized in order to validate the model predictions.

DEDICATION

To my parents

To my grandparents

To my sister

To my professors

To my friends

ACKNOWLEDGEMENTS

I would like to express my gratitude to my research advisor, Dr. Micah Green, and my research co-advisor, Dr. Mohammad Naraghi, for their constant support, feedback and guidance throughout my research, and for giving me an opportunity to work on such a fascinating and thought-provoking topic. Their expertise, critique, and opinion has been extremely helpful to me during this study. I am grateful to Dr. Yossef Elabd for serving on my committee. I would like to thank my colleague, Kai Morikawa, who assisted me with the experimental section of this thesis. I really appreciate the support that I got from my friends and colleagues, as well as the faculty and staff at Texas A&M University. Finally, I want to thank my entire family for their constant encouragement and motivation during the entire phase of my MS degree.

CONTRIBUTORS AND FUNDING SOURCES

Contributors

This work was supported by a thesis committee consisting of Dr. Micah Green of the Department of Chemical Engineering (advisor), Dr. Mohammad Naraghi of the Department of Aerospace Engineering (co-advisor), and Dr. Yossef Elabd of the Department of Chemical Engineering (committee member).

The analyses depicted in Chapter III and Chapter IV (Section 4.2.) were conducted in part by Kai Morikawa of the Department of Aerospace Engineering.

All other work conducted for the thesis was completed by the student independently.

Funding Sources

This work was made possible in part by the National Science Foundation under Grant Number CMMI-153804.

NOMENCLATURE

R - Radius of the polymer jet

v - Local velocity of the polymer jet

$\dot{V}$ - Flowrate of the polymer jet

ρ - Density of the polymer

g - Acceleration due to gravity

F_T - Viscoelastic tensile force in the polymer jet

γ - Surface tension of the polymer

σ - Surface charge density of the polymer

ε_0 - Vacuum permittivity

ε - Local permittivity of the polymer

E_t - Component of the electric field tangential to the polymer jet surface

K - Electrical conductivity of the polymer

I - Electric current through the polymer jet

E - Electric field acting on the polymer jet

E_∞ - Electric field due to the voltage applied between the syringe nozzle and the collector

V - Applied potential difference between the syringe nozzle and the collector

R_0 - Initial radius of the polymer jet

z - Distance along the direction of electrospinning

d - Separation distance between the syringe nozzle and the collector

C_p - Heat capacity of the polymer

T - Temperature of the polymer jet

h - Convective heat transfer coefficient

T_∞ - Surrounding temperature

Q - Volumetric heat source

k_{air} - Thermal conductivity of air

δ_{air} - Kinematic viscosity of air

A - Cross-sectional area of the polymer jet

v_{air} - Speed of the cooling air

τ_p - Polymeric stress tensor

α - Mobility factor of the polymer

λ_0 - Relaxation time of the polymer

T_0 - Jet temperature at the inlet/syringe nozzle (reference temperature)

η_{p0} - Polymer contribution to the zero-shear-rate viscosity at the reference temperature

$f(T)$ - Temperature dependence of the zero-shear-rate viscosity

$\eta_0(T)$ - Zero-shear-rate viscosity at temperature T

$\eta_0(T_0)$ - Zero-shear-rate viscosity at inlet/syringe nozzle temperature T_0

ΔH - Activation energy of flow

R_{ig} - Ideal gas constant

$\tau_{p,zz}$ - Polymeric stress in the axial direction

$\tau_{p,rr}$ - Polymeric stress in the radial direction

τ_{zz} - Total stress in the axial direction

τ_{rr} - Total stress in the radial direction

η_{s0} - Solvent contribution to the zero-shear-rate viscosity at the reference temperature

Re - Reynolds number

Bo - Bond number

Ca - Capillary number

F_e - Electrostatic force parameter

β_E - Dielectric constant ratio

Pe_c - Peclet number (for electrical conductivity)

χ - Dimensionless distance from syringe nozzle to collector

Pe - Peclet number (for thermal conductivity)

Na - Nahme-Griffith number

Bi_L - Local Biot number (takes into account the evolution of the heat transfer coefficient in the axial direction)

Q_p - Dimensionless volumetric heat source

Bi - Biot number

β - Ratio of solvent to zero-shear-rate viscosity

De - Deborah number

Γ - Temperature factor

h_0 - Heat transfer coefficient evaluated at the syringe nozzle

k - Thermal conductivity of the polymer

K - Electrical conductivity of the polymer

H - Vertical distance between heat lamp and glass plate

R_{final} - Final radius of the polymer jet

Δa - Dimensionless length over which heat is provided to the polymer jet

TABLE OF CONTENTS

Page

Page

LIST OF FIGURES

Page

LIST OF TABLES

Page

CHAPTER I

INTRODUCTON

1.1. Motivation and research objectives

Over the past few decades, micro/nanoscale fibers have attracted major attention due to their remarkable properties and wide range of potential applications. Some of their numerous fascinating characteristics include - high surface area to volume ratio, small pore size, tunable mechanical strength to weight ratio, and flexibility in surface functionalities.[1-3] Due to these properties, they find use in many attractive applications such as:

- Filtration: Micro/nanofibers can function as excellent filter media. The large surface area per unit volume of the fibers provides ample filter-medium interface to reject undesired particles.[4,5]
- Tissue engineering: Micro/nanofibers can be used to produce tissue scaffolds with surface properties and architecture that supports cell attachment, migration, growth, and ultimately tissue maturation.[6,7]
- Drug delivery: The inherently high surface area to volume ratio of micro/nanofibers can enhance cell attachment, drug loading, and mass transfer properties.[8]
- Energy storage: Micro/nanofibers can be used for manufacturing battery membranes, and therefore find application as a material for energy storage.[2,8-11]

However, despite such promising applications, scalable methods to produce micro/nanofibers are still in their infancy. There have been efforts to produce polymeric micro/nanofibers in large quantities via solution-based electrospinning. But, these methods are generally not considered "green", due to release of toxic solvent vapor. The alternative solvent-free approach - melt electrospinning, often leads to the production of thick fibers. This is partly because of the fact that a polymer melt has a high viscosity and a low charge density (which results in a low electrostatic force on the polymer jet).[12] In addition, rapid heat exchange between the polymer and the environment often leads to the solidification of the jet, thereby preventing major jet drawing by the electric field.[13] Hence, through our research, we propose to address these issues so that it could be possible to manufacture micro/nanofibers in an environment-friendly and industrially scalable manner.

1.2. Organization of the thesis

This thesis is divided into five chapters. In Chapter II, we discuss the process of electrospinning with particular focus on melt electrospinning. Here, we introduce our idea for modifying the process of melt electrospinning so as to achieve the proposed objective of our research. In Chapter III, we describe the main modeling and experimental methods that were used in our research. Next, in Chapter IV, we present the results of our effort. In this chapter, we demonstrate that our model establishes the significance of our novel concept, and the experimental work proves that our idea can be physically implemented

in order to obtain desirable results. Finally, In Chapter V, we present the conclusions of our work, and also suggest a possible direction for future research.

CHAPTER II

ELECTROSPINNING

2.1. Introduction to electrospinning

Industrially, micro/nanoscale fibers are produced via electrospinning - a fiber production method which uses electric force to draw charged threads of polymer solutions or polymer melts up to fiber diameters in the sub-micron range.[14,15]

A typical electrospinning setup comprises of three major components as can be seen from Figure 1.[16] The first component is the feeding unit which consists of the syringe and the syringe pump. The next component is a high voltage power supply which is used to generate an electric field. Finally, the last component is the collector plate which is used for collecting the electrospun fiber.[17] Before electrospinning, the polymer is either completely dissolved in a suitable solvent or it is melted, and then placed in the syringe. The syringe pump is then used for pushing the fluid out of the syringe nozzle. Next, using the power supply, a high voltage difference is applied between the syringe nozzle and the collector plate. Once the fluid flows out of the syringe nozzle, it comes under the influence of the electric field, and starts developing electrostatic charges. The fluid at the nozzle is held by its own surface tension, until such a point when the electrostatic forces developed in the fluid overcome its surface tension. Subsequently, it assumes a conical shape (known as the Taylor cone) before a stream of fluid vents out. The jet elongates in the electric field before eventually getting deposited on the collector.[18]

An electrospinning process typically has two stages - a stable jet stage and an instability stage, as depicted in Figure 1.[16] In the first stage, the jet accelerates in a straight trajectory for a certain distance from the syringe nozzle. The jet profile does not vary with time. This is followed by the second stage in which the jet is observed to exhibit a distinct "whipping motion". This chaotic motion often arises due to bending instabilities that are produced in the jet as a result of the electrostatic charges.[19]

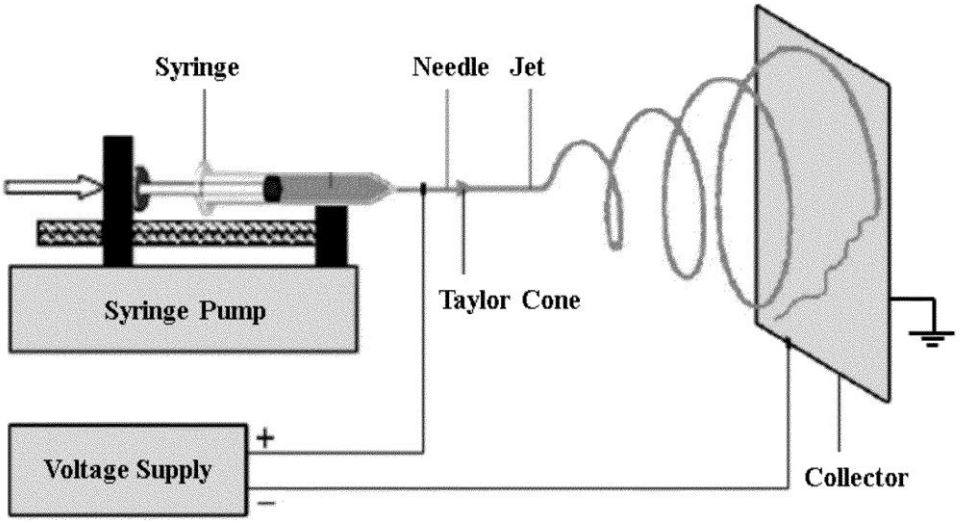

Figure 1: Typical setup for electrospinning.[16]

Finally, depending upon the physical state of the polymer used, the process of electrospinning is categorized as - solution electrospinning (in which a polymer solution is used), and melt electrospinning (in which the polymer is in its melt state). These will be elaborated in the following sections.

2.2. Solution electrospinning

Solution electrospinning is the more popular electrospinning technique for fabricating sub-micron fibers. For solution electrospinning, the fluid present inside the syringe nozzle is a polymer which had been thoroughly dissolved in a solvent. In this process, as the jet forms near the nozzle and travels towards the collector, the solvent evaporates and dry sub-micron sized fibers are obtained on the collector.[20] In the stable jet region, the fiber elongates under the influence of the electric field. Once the bending instabilities set in, the chaotic whipping motion of the jet allows the polymer chains within to stretch and slide past each other, which results in the formation of fibers having a small diameter.[21]

However, in this process, a large amount of solvent is introduced to the atmosphere (as much as 5 - 10 times the mass of the produced fibers) which may cause environmental pollution and demand a safe ventilation measure in order to avoid any health issue.[22-24] Other major challenges for solution electrospinning include recovery of organic solvents, residual toxic solvents in the fibers, and small pores in the fibers (due to solvent evaporation or unintended phase separation).[25,26] More importantly, solution electrospinning is unsuitable for processing many relevant commodity polymers.

Due to these drawbacks of solution electrospinning, significant study has been devoted to melt electrospinning - an alternative solvent-free approach for manufacturing sub-micron sized fibers.

2.3. Melt electrospinning

Figure 2 shows a schematic representation of the process of melt electrospinning. Here, the fluid present in the syringe is typically a polymer in its melt state. This process differs from solution electrospinning in another aspect - the whipping instability in melt electrospinning is much less pronounced as compared to solution electrospinning. This is mainly because a melt has a lower charge density (which results in a lower magnitude of electrostatic force) and a higher viscosity (which helps the melt to resist the bending motion).[27]

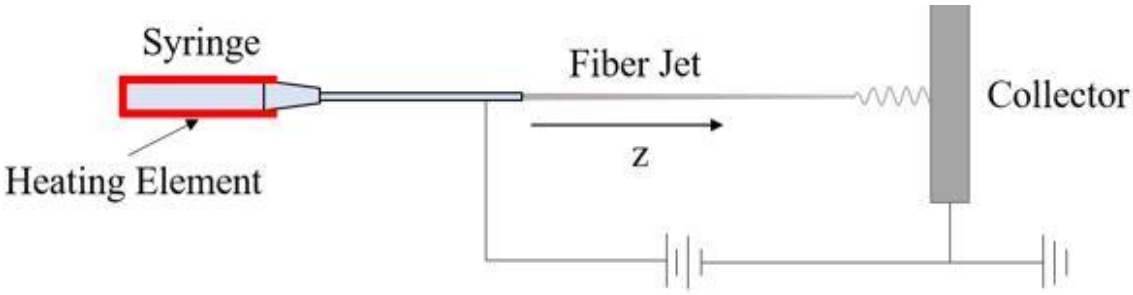

Figure 2: Schematic of a typical setup for melt electrospinning.

Several parameters in the melt electrospinning process play a vital role in determining the fiber diameter.[28,29] These include:

- Electric field strength:
    - Lyons *et al.* researched the effect of the electric field strength on the collected fiber diameter of select electrospun polymers. These studies indicated that the larger electric field strengths produced polymers with smaller fiber diameters.[30]

- Long *et al.* explored the influence of the collector distance on the fiber diameter. Fiber diameter initially decreases on increasing collector distance up to a certain extent. Then the fiber diameter increases on further increasing the collector distance. There are two factors influencing this phenomenon - the fiber stretching time and the electric force experienced by the fiber. What happens is, initially, on increasing the collector distance, the effect of increasing the fiber stretching time is more significant compared to the effect of diminishing electric force experienced by the fiber, and therefore, the fiber diameter decreases. After a certain distance downstream, the effect of the diminishing electric force felt by the fiber dominates the effect of prolonging the fiber stretching time, which leads to an increase in the fiber diameter.[31]

- Flow rate:
  - Studies show that flow rate is directly proportional to fiber diameter. In Hutmatcher's experiment, at constant voltage and spinning distance, on operating at flow rates of 5, 10, and 20 μLh^{-1}, fibers with different average diameters of 6.6, 12.6, and 20.3 μm were obtained.[32]

- Air temperature:
  - Viscosity is an important factor in determining the fiber diameter in the electrospinning process. The temperature of air in the spinning chamber has a significant influence on the viscosity of the polymer melt. Generally,

the viscosity will reduce with an increase in the spinning temperature, and consequently the fiber diameter will decrease.[33-35]

2.4. Challenges in the process of melt electrospinning

Although melt electrospinning has certain advantages over solution electrospinning, it comes with its own set of challenges. A polymer melt has a high viscosity and a low charge density. The former lowers the stretchability of the jet, while the latter results in a low electrostatic force on the jet.[12,36] In addition, rapid heat exchange between the jet and the environment often solidifies the jet in the vicinity of the Taylor cone, which prevents major jet drawing by the electric field.[13] Due to this, fibers produced using melt electrospinning often tend to be thicker compared to solution electrospinning.

2.5. Downstream volumetric heat

In order to overcome some of the challenges faced by current melt electrospinning systems, we propose to incorporate a new means of extending the melt thinning region - through a downstream volumetric heat source, which can be manipulated by the system geometry. This volumetric heat source term is active at every point within the fiber volume and has units of W/m^3. Rather than a simple empirical approach, we utilize a model to predict how our novel experimental setup can be tailored to alter the fiber radius dynamics. In principle, the volumetric heat source can be treated as a step function in the region where we turn on the heat and zero elsewhere as shown in Figure 3.

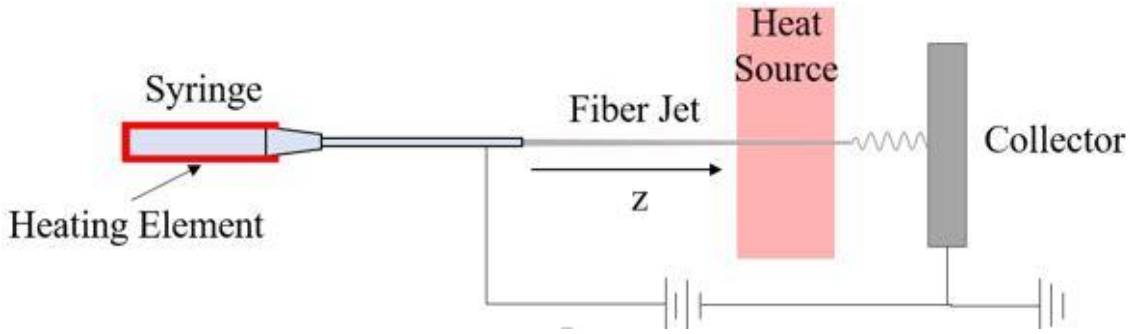

Figure 3: Schematic of our setup for melt electrospinning PLA.

This volumetric heat source could stem from the interaction of the polymer (or a filler) with an applied electromagnetic field. If the penetration depth of the field is larger than the radius of the fiber, the field would be able to interact across the cross-sectional area of the fiber rather than at the surface only. In many cases, the polymer may require additives in order to be field responsive. One can envision several different experimental scenarios where downstream volumetric heating is possible, including the following:

(i) Microwave fields interacting with embedded conductive nanoscale inclusions in the polymer.[37]

(ii) Laser radiation interacting with dyes embedded in the polymer.[38]

(iii) Magnetic fields interacting with superparamagnetic nanoparticle additives in the polymer.[39]

Note, of course, that such additives may change the physical properties of the polymer, and would need to be accounted for.

In our research, we utilize both, a modeling and an experimental approach to demonstrate the utility of downstream volumetric heating in the process of melt electrospinning. Our model predicts the fiber radius as a function of distance from the syringe nozzle. In addition, we have also investigated different trends by varying the surrounding air temperature, the magnitude of downstream heat, as well as the region where downstream heat is provided. Experiments are conducted to validate the predictions of the model. For the experiments, downstream heat is provided using an infrared heat lamp placed at various distances to simulate different magnitudes of heat. The results of initial jet profile and final fiber radius are compared for various magnitudes of downstream heat.

CHAPTER III

MODEL AND EXPERIMENT

3.1. Model

3.1.1. Background

In conventional electrospinning, the polymer jet undergoes rapid initial thinning in a stable trajectory. Further downstream, bending instabilities cause a whipping motion which further thins the jet prior to its arrival and solidification on a collector plate.[40-44] For the particular case of melt-electrospinning, this whipping movement is not nearly as pronounced as it is in solution electrospinning. This is because of the large fiber diameter of the former because of which the polymer jet experiences little or no bending instabilities.[27] This increases the importance of optimizing the thinning of the polymer melt in the stable jet region. Therefore, in this paper, we model the jet as if it had a stable trajectory right from the syringe nozzle to the collector.

From a modeling point of view, the stable jet region has been extensively examined in previous studies. Spivak and Dzenis developed a 1-D model with a power law fluid.[45] Hohman *et al*. refined this model by introducing the concept of a "leaky dielectric" in order to account for the interaction of the surface charges in the jet with the external applied electric field.[43,44] Feng incorporated the Giesekus constitutive model to account for the viscoelastic behavior of polymers.[46,47] Carroll and Joo verified the predictions of Feng's model by comparing it to numerous experimental results.[19] A corresponding non-

isothermal model, particularly for simulating the process of polymer melt-electrospinning, was proposed by Zhmayev *et al*.[13] This study utilizes the model used by Zhmayev *et al*., and extends it to examine the effect of adding a downstream volumetric heat source.

3.1.2. Governing equations

The present simulation model for the stable jet trajectory is developed by fully coupling the conservation of mass, momentum, charge, and energy equations at steady state, along with an electric field equation, and a viscoelastic constitutive model. A thin filament (1-D) approximation has been utilized in order to obtain a simpler solution. That is, all the model variables across the radial direction are averaged. The crystallization rate of PLA is slow, and the residence time of polymer melt is short during electrospinning, such that melt electrospun PLA is mostly amorphous. Thus, polymer crystallization is not considered in the current study.

The governing equations for non-isothermal simulations have been presented by Zhmayev *et al*.[13] We follow their basic format and modify as needed for our case:

Mass: $\pi R^2 v = \dot{V}$ (1)

Momentum: $\rho v v' = \rho g + \frac{F_T'}{\pi R^2} + \frac{\gamma R'}{R^2} + \frac{\sigma \sigma'}{\varepsilon_0} + (\varepsilon - \varepsilon_0) E_t E_t' + \frac{2\sigma E_t}{R}$ (2)

Charge: $\pi R^2 K E_t + 2\pi R v \sigma = I$ (3)

Electric field: $E \approx E_\infty = \frac{2V}{\left[\left(R_0 + 2z - \frac{z^2}{d}\right) ln\left(1 + \frac{4d}{R_0}\right)\right]}$ (4)

Tangential projection of electric field: $E_t = \frac{E}{\sqrt{1+(R')^2}}$ (5)

In the above set of equations, R is the radius of the polymer jet, v is the local velocity of the jet, $\dot{V}$ is the flowrate of the polymer jet, ρ is the density of the polymer, g is the acceleration due to gravity, F_T is the viscoelastic tensile force in the jet (computed from the constitutive Giesekus equation), γ is the surface tension of the polymer, σ is the surface charge density of the polymer, ε_0 is the vacuum permittivity, ε is the local permittivity of the polymer, E is the electric field acting on the polymer jet, E_t is the component of the electric field tangential to the jet surface, K is the electrical conductivity of the polymer, I is the electric current, E_∞ is the electric field applied between the syringe nozzle and the collector, V is the applied potential difference between the syringe nozzle and the collector plate, R_0 is the initial radius of the polymer jet, d is the syringe nozzle-to-collector separation distance, and z denotes the direction of electrospinning. Primes indicate derivatives with respect to z.

In our case, the conservation of charge equation considers both the components of the current carried by jet - the charge convection on the surface of the jet, and the conduction within it.[19] (Zhmayev *et al.* had assumed a non-conductive jet.[13])

Further, in order to validate the use of Equation (4) and Equation (5) for representing the electric field in our case, we compared the values of the tangential component of electric field obtained from Equation (5) with those obtained by using COMSOL finite element solver.

In order to obtain the numerical values of the tangential component of electric field as a function of *z*, the given system of equations was solved using an implicit time stepper in MATLAB to get the values of *R* and *R'*, where *R'* is the derivative with respect to *z*. Then, we plug in the values of *V*, R_0, *d*, and the values of *R'* obtained above, into Equation (5).

Now, using COMSOL finite element solver, we simulated the electric field acting on a polymer melt jet between a syringe and a collector plate under the same processing conditions. After processing the data, we computed the values of the tangential component of this electric field in order to compare against the values obtained from Equation (5).

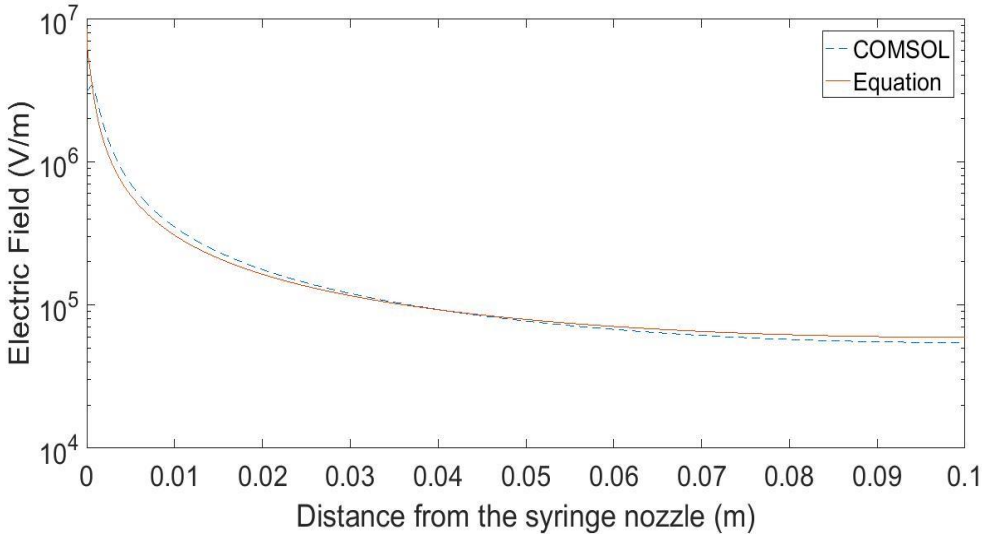

Figure 4: Comparison of electric field obtained using COMSOL, and that obtained using Equation (5) from the paper.

As seen from Figure 4, a close overlap between the two lines justifies the use of Equation (4) and Equation (5) for representing the electric field between a syringe and collector plate, for our case.

Next, we extend the existing model by Zhmayev *et al*. by incorporating a volumetric heat source term in the conservation of energy relation. This has been computed by performing a 1-D energy shell balance on a disk-shaped fluid element. The change in internal energy of the fluid element is balanced with viscous heating, radial convection heat loss to the surroundings, and the volumetric heat added to the system. Another possible heat source term arising because of heat released due to crystallization is not considered in this study. The resulting equation is:

$$\text{Energy: } \rho C_p v T' = \frac{v' F_T}{\pi R^2} - \frac{2h(T-T_\infty)}{R} + Q \tag{6}$$

Here, C_p is the polymeric heat capacity, T is temperature of the polymer jet, h is the convective heat transfer coefficient, T_∞ is the external air temperature, and Q is the volumetric heat source. As stated earlier, primes indicate derivatives with respect to z, which is the direction of electrospinning.

The heat transfer coefficient is determined from an empirical relation by Matsuo and Kase.[48] This relation has been employed in previous melt electrospinning studies:

$$h = 0.388 k_{air} \left(\frac{v}{\delta_{air} A}\right)^{1/3} \left(1 + \left(\frac{8 v_{air}}{v}\right)^2\right)^{1/6} \tag{7}$$

Here, k_{air}, δ_{air}, and v_{air} are the thermal conductivity, kinematic viscosity, and the speed of the cooling air, respectively, and A is the cross-sectional area of the polymer jet.

The non-isothermal constitutive model used for describing the viscoelastic behavior of the polymer melt has been incorporated here in the same manner as done by Zhmayev *et al*.[13]

The polymeric stress tensor, τ_p, used to account for the viscoelastic behavior of the melt, is described by the Giesekus constitutive model modified to its non-isothermal form via time-temperature superposition.[49]

$$\tau_p + \alpha \frac{\lambda_0 T_0}{\eta_{p_0} T}\{\tau_p.\tau_p\} + \lambda_0 f(T)\frac{T_0}{T}\left[\tau_{p(1)} - \tau_p \frac{Dln(T)}{Dt}\right] = -\eta_{p_0} f(T)\dot{\gamma} \quad (8)$$

Here, α is the mobility factor, reference temperature T_0 is the temperature of the polymer jet at the inlet/syringe nozzle, λ_0 and η_{p0} are the polymer relaxation time and the polymer contribution to the zero-shear-rate viscosity at the reference temperature, respectively, *D/Dt* denotes the material derivative, and *f(T)* represents the temperature dependence of the zero-shear-rate viscosity, defined as:

$$f(T) = \frac{\eta_0(T)}{\eta_0(T_0)} = exp\left[\frac{\Delta H}{R_{ig}}\left(\frac{1}{T} - \frac{1}{T_0}\right)\right] \quad (9)$$

Here, $\eta_0(T)$ is the zero-shear-rate viscosity at the polymer jet temperature T, $\eta_0(T_0)$ is the zero-shear-rate viscosity at inlet/syringe nozzle temperature T_0, ΔH is the activation energy of flow, and R_{ig} is the ideal gas constant. The two non-vanishing components of the polymeric stress can finally be written as:

$$\tau_{p,zz} + \alpha \frac{\lambda_0 T_0}{\eta_{p_0} T}{\tau_{p,zz}}^2 + \lambda_0 f(T)\frac{T_0}{T}\left[v\tau_{p,zz}' - 2v'\tau_{p,zz} - \frac{v\tau_{p,zz}T'}{T}\right] = 2\eta_{p_0} f(T)v' \quad (10)$$

$$\tau_{p,rr} + \alpha \frac{\lambda_0 T_0}{\eta_{p_0} T}{\tau_{p,rr}}^2 + \lambda_0 f(T)\frac{T_0}{T}\left[v\tau_{p,rr}' + v'\tau_{p,rr}\right] = -\eta_{p_0} f(T)v' \quad (11)$$

In the above equations, $\tau_{p,zz}$ is the polymeric stress in the axial direction, and $\tau_{p,rr}$ is the polymeric stress in the radial direction.

The total axial and radial normal stresses under non-isothermal conditions are:

$$\tau_{zz} = \tau_{p,zz} + 2\eta_{s_0} f(T) v' \tag{12}$$

$$\tau_{rr} = \tau_{p,rr} - \eta_{s_0} f(T) v' \tag{13}$$

Here, τ_{zz} is the total axial stress, τ_{rr} is the total normal stress, η_{s0} is the solvent contribution to the zero-shear rate viscosity at the reference temperature. Again, primes indicate derivatives with respect to *z*, which is the direction of electrospinning.

Finally, the viscoelastic tensile force in the polymer jet is given by:

$$F_T = \pi R^2 (\tau_{zz} - \tau_{rr}) \tag{14}$$

3.1.3. Characteristic quantities

Length: R_0

Velocity: $v_0 = \frac{\dot{V}}{\pi {R_0}^2}$

Electric field: $E_0 = E(0) = \frac{2V}{R_0 ln\left(1+\frac{4d}{R_0}\right)}$

Surface charge density: $\sigma_0 = \varepsilon_0 E_0 = \frac{IR_0}{2\dot{V}}$

Stress: $\tau_0 = \frac{\eta_0(T_0) v_0}{R_0}$

Temperature: T_0 and $\Delta T_{Rh} = \left| \frac{\eta_0(T)}{\frac{\partial \eta_0(T)}{\partial T}} \right|_{T = T_0}$

Here, ΔT_{Rh} is the temperature change which significantly alters the rheological properties of the fluid. Also, in order to simplify the calculations, dimensionless temperature is defined as:

$$\theta = \frac{T - T_0}{\Delta T_{Rh}}$$

Using these characteristic quantities, we can non-dimensionalize each of the governing equations in our model.

3.1.4. Non-dimensionalization

The final set of non-dimensionalized governing equations are as presented below:

Continuity:

$$R^2 v = 1 \tag{15}$$

Momentum:

$$Revv' = Bo + \frac{\left(R^2(\tau_{zz} - \tau_{rr})\right)'}{R^2} + \frac{R'}{CaR^2} + F_e\left(\sigma\sigma' + \beta_E E_t {E_t}' + \frac{2\sigma E_t}{R}\right) \tag{16}$$

Charge:

$$\sigma = R - \frac{R^3 E_t}{Pe_c} \tag{17}$$

$$\sigma' = R' - \frac{3R^2 R' E_t + R^3 {E_t}'}{Pe_c} \tag{18}$$

Electric field:

$$E_t = \frac{1}{\left[\left(1+2z-\frac{z^2}{\chi}\right)(1+(R')^2)^{0.5}\right]} \tag{19}$$

$$E_t{}' \approx \frac{-2+\frac{2z}{\chi}}{\left(1+2z-\frac{z^2}{\chi}\right)^2(1+(R')^2)^{0.5}} \tag{20}$$

Energy:

$$Pev\theta' = Nav'(\tau_{zz}-\tau_{rr}) - \frac{2Bi_L}{R}(\theta-\theta_\infty) + Q_p \tag{21}$$

$$Bi_L = Bi\left(\frac{v}{R^2}\right)^{1/3}\left(\frac{1+(8v_{air}/v)^2}{1+(8v_{air})^2}\right)^{1/6} \tag{22}$$

Here, Bi_L is the local Biot number, which takes into account the evolution of the heat transfer coefficient in the axial direction.

Constitutive:

$$\tau_{zz} = \tau_{p,zz} + 2\beta f(\theta)v' \tag{23}$$

$$\tau_{rr} = \tau_{p,rr} - \beta f(\theta)v' \tag{24}$$

$$\tau_{p,zz} + \frac{De\Gamma}{(\theta+\Gamma)}\left(\frac{\alpha\tau_{p,zz}{}^2}{(1-\beta)} + f(\theta)\left[v\tau_{p,zz}{}' - 2v'\tau_{p,zz} - \frac{v\tau_{p,zz}\theta'}{(\theta+\Gamma)}\right]\right) = 2(1-\beta)f(\theta)v' \tag{25}$$

$$\tau_{p,rr} + \frac{De\Gamma}{(\theta+\Gamma)}\left(\frac{\alpha\tau_{p,rr}{}^2}{(1-\beta)} + f(\theta)\left[v\tau_{p,rr}{}' + v'\tau_{p,rr}\right]\right) = -(1-\beta)f(\theta)v' \tag{26}$$

$$f(\theta) = exp\left[\frac{\Delta H}{R_{ig}\Delta T_{Rh}}\left(\frac{1}{(\theta+\Gamma)} - \frac{1}{\Gamma}\right)\right] \tag{27}$$

$$f'(\theta) = exp\left[\frac{\Delta H}{R_{ig}\Delta T_{Rh}}\left(\frac{1}{(\theta+\Gamma)} - \frac{1}{\Gamma}\right)\right]\left(\frac{\Delta H}{R_{ig}\Delta T_{Rh}}\right)\left(\frac{-1}{(\theta+\Gamma)^2}\right)\theta' \quad (28)$$

Here, β represents solvent to zero-shear-rate viscosity ratio. In contrast to previous studies on modeling of melt electrospinning,[13] we argue that the value of β should be equal to 0, as no solvent is actually present in the melt. In our simulations, we simply set this parameter to a small value such that our simulations converge on the solution as $\beta \rightarrow 0$.

Note that all quantities used from this point onwards are dimensionless, but the same symbols are used for convenience. Also note that in the aforementioned set of equations, the following quantities are functions of *z*:

R, v, τ_{zz}, τ_{rr}, σ, E_t, θ, Q_p, $\tau_{p,zz}$, $\tau_{p,rr}$, and $f(\theta)$.

A number of dimensionless groups appear while deriving the above non-dimensional set of equations. These are presented below:

Dimensionless distance from syringe nozzle to collector: $\chi = \frac{d}{R_0}$

Biot number: $Bi = \frac{h_0 R_0}{k}$

Bond number: $Bo = \frac{\rho g {R_0}^2}{\eta_0 v_0}$

Capillary number: $Ca = \frac{v_0 \eta_0}{\gamma}$

Deborah number: $De = \frac{\lambda_0 v_0}{R_0}$

Dielectric constant ratio: $\beta_E = \frac{\varepsilon}{\varepsilon_0} - 1$

Electrostatic force parameter: $F_e = \frac{\varepsilon_0 {E_0}^2 R_0}{V_0 \eta_0}$

Nahme-Griffith number: $Na = \frac{\eta_0 {v_0}^2}{k \Delta T_{Rh}}$

Peclet number (for thermal conductivity): $Pe = \frac{\rho C_p R_0 v_0}{k}$

Peclet number (for electrical conductivity): $Pe_c = \frac{2\varepsilon_0 v_0}{k R_0}$

Ratio of solvent to zero-shear-rate viscosity: $\beta = \frac{\eta_s(T_0)}{\eta_0(T_0)}$

Reynolds number: $Re = \frac{\rho v_0 R_0}{\eta_0}$

Temperature factor: $\Gamma = \frac{T_0}{\Delta T_{Rh}}$

Dimensionless volumetric heat source: $Q_p = \frac{Q {R_0}^2}{k \Delta T_{Rh}}$

Here, h_0 is the heat transfer coefficient evaluated at the syringe nozzle, and k is the thermal conductivity of the fluid.

3.1.5. Boundary conditions

On rearranging the system of equations presented in the previous section, the problem can be reduced to a set of five first order ordinary differential equations (ODEs) ready for numerical analysis. The following boundary conditions are required to appropriately address the problem. The conditions on the normal polymeric stresses rely on the

assumption that the polymer is sufficiently relaxed at the inlet, and hence, as in previous studies, the initial stresses are assumed to be those of a Newtonian fluid.[19,46,47]

$$\tau_{p,zz}|_{z=0} = 2(1 - \beta)f(\theta)v' \tag{29}$$

$$\tau_{p,rr}|_{z=0} = -(1 - \beta)f(\theta)v' \tag{30}$$

At the inlet, that is, at z = 0, the temperature of the polymer jet is equal to the syringe nozzle temperature. Therefore, after non-dimensionalization, this condition can be expressed as:

$$\theta|_{z=0} = 0 \tag{31}$$

Similarly, at z = 0, the radius of the polymer jet is equal to the radius of the syringe nozzle. In the non-dimensional form, this is written as:

$$R|_{z=0} = 1 \tag{32}$$

For the final boundary condition, past electrospinning models have utilized an underlying assumption of the balance of inertial and electrical forces in the asymptotic region.[19,45-47,50] However, under non-isothermal conditions, this does not hold true for highly viscoelastic fluids such as polymer melts, as they exhibit high tensile forces throughout the spinning region. Zhmayev *et al*. proposed a new initial thinning condition for fluids with low electrical conductivity and high viscosity (such as polymer melts) based on a force balance near the syringe nozzle. Since the fluid at the syringe nozzle is assumed to be nearly Newtonian, the following terms must be balanced: Newtonian stresses, surface tension, and electric driving force. This results in the following algebraic relationship (in

the non-dimensional form) that can be solved to obtain $R'(0)$, and hence the last needed boundary condition which we will be incorporating in our model.[13]

$$\left[\frac{6}{R^4}(R')^2 + \left(\frac{1}{CaR^2} + F_e R\right)R' + \frac{2F_e}{\sqrt{1+(R')^2}} + \left(1 - \frac{\beta_E}{\sqrt{1+(R')^2}}\right)\right]_{z=0} = 0 \quad (33)$$

With the assumptions of the current model we have been able to reduce what would have been a boundary value problem of seven coupled ODEs to an initial value problem of five coupled ODEs. As a result, the current approach has led to a stable system that converges for a wide range of parameters, and easily covers the experimentally relevant window of non-isothermal processing conditions.

3.1.6. Numerical solution

The current model has been formulated as an initial value problem of five coupled first order ODEs, and has been solved numerically using an implicit solver in MATLAB. In order to gain additional insight into the electrospinning process, we have also investigated general trends in response to changing the surrounding air temperature, the magnitude of downstream heat, and the region over which the heat will be provided.

The material properties of PLA used in the simulation are similar to those used by Zhmayev *et al*.,[13] and are presented in Table 1.

Table 1: Material properties of PLA.

Properties	**Values**
Zero-shear-rate viscosity (at 180 ºC) (η_0)	1320 Pa.s
Relaxation time (at 180 ºC) (λ_0)	0.1 s
Activation energy of flow ($\Delta H/R_{ig}$)	9060 K
Density (ρ)	1240 kg/m^3
Heat capacity (C_p)	1800 J/kg.K
Thermal conductivity (k)	0.2 W/m.K
Electrical conductivity (K)	10^{-10} S/m
Surface tension (γ)	0.0435 N/m
Ratio of solvent to zero-shear-rate viscosity (β)	0.001
Mobility factor (α)	0.015
Dielectric constant ratio ($\varepsilon/\varepsilon_0$)	3.1

The reference set of dimensionless groups which have been used in the simulations, is based on PLA properties and typical experimental conditions (V = 20 kV, d = 0.1 m, R_0 = 0.5 mm, and $\dot{V}$ = 0.044 mL/minute) as used by Zhmayev *et al*.,[13] and is listed in Table 2.

Table 2: Typical values of dimensionless numbers and parameters used for PLA simulations.

Bi	0.0103
De	0.0270
Bo	0
Re	2.564×10^{-6}
Ca	4.264
Na	2.632×10^{-5}
$\mathbf{F_e}$	3.324
Γ	18.193
Pe	4.770
$\mathbf{Pe_c}$	0.294

It is important to note that the model mainly simulates melt-electrospinning using PLA as the polymer, but PCL was chosen for the experiment because it is simpler to melt-electrospin PCL due to its relatively low melting point. So, in order to validate the model, we have simulated certain results with PCL as the polymer, so as to compare it with the experiment. The material properties of PCL used in these simulations are presented in Table 3.

Table 3: Material properties of PCL.[13,51-54]

Properties	**Values**
Zero-shear-rate viscosity (at 100 ºC) (η_0)	1900 Pa.s
Relaxation time (at 100 ºC) (λ_0)	0.019 s
Activation energy of flow ($\Delta H/R_{ig}$)	7938.4 K
Density (ρ)	1145 kg/m^3
Heat capacity (C_p)	1340 J/kg.K
Thermal conductivity (k)	0.14 W/m.K
Electrical conductivity (K)	9.5×10^{-9} S/m
Surface tension (γ)	0.0435 N/m
Ratio of solvent to zero-shear-rate viscosity (β)	0.001
Mobility factor (α)	0.015
Dielectric constant ratio ($\varepsilon/\varepsilon_0$)	2.9

The reference set of dimensionless groups which have been used in the simulations is based on PCL properties and experimental conditions as mentioned in Section 3.2.2. of this chapter, and is listed in Table 4.

Table 4: Typical values of dimensionless numbers and parameters used for PCL simulations.

Bi	0.424
De	1.14
Bo	0
Re	5.785×10^{-6}
Ca	1048.276
Na	0.446
F_e	0.0254
Γ	21.283
Pe	105.209
Pe_c	0.1122

3.2. Experiment

3.2.1. Experimental setup

PCL was purchased from Polysciences Inc. (MW = 37,000). The PCL was used as purchased. It was heated in a 10 mL polystyrene syringe, with an 18 gauge (~400 μm radius) needle with 0.5 inch length. The heating mechanism used was a syringe heater (New Era Pump Systems, HEATER-KIT-1LG). A high voltage power supply (Acopian, N030HP1) was used to provide the electric field. A heat lamp (McMaster Carr, Product No. 3343K11) with a halogen light bulb having a power of 600 W (McMaster Carr, Product No. 1535K96) was used to act as the downstream heat source. This heat lamp was

used at various distances (H) to simulate different magnitudes of heat. An aluminum plate (3.5” x 2.5”) wrapped in aluminum foil was used as the collector. Figure 5 shows the schematic of the setup used for our experiment.

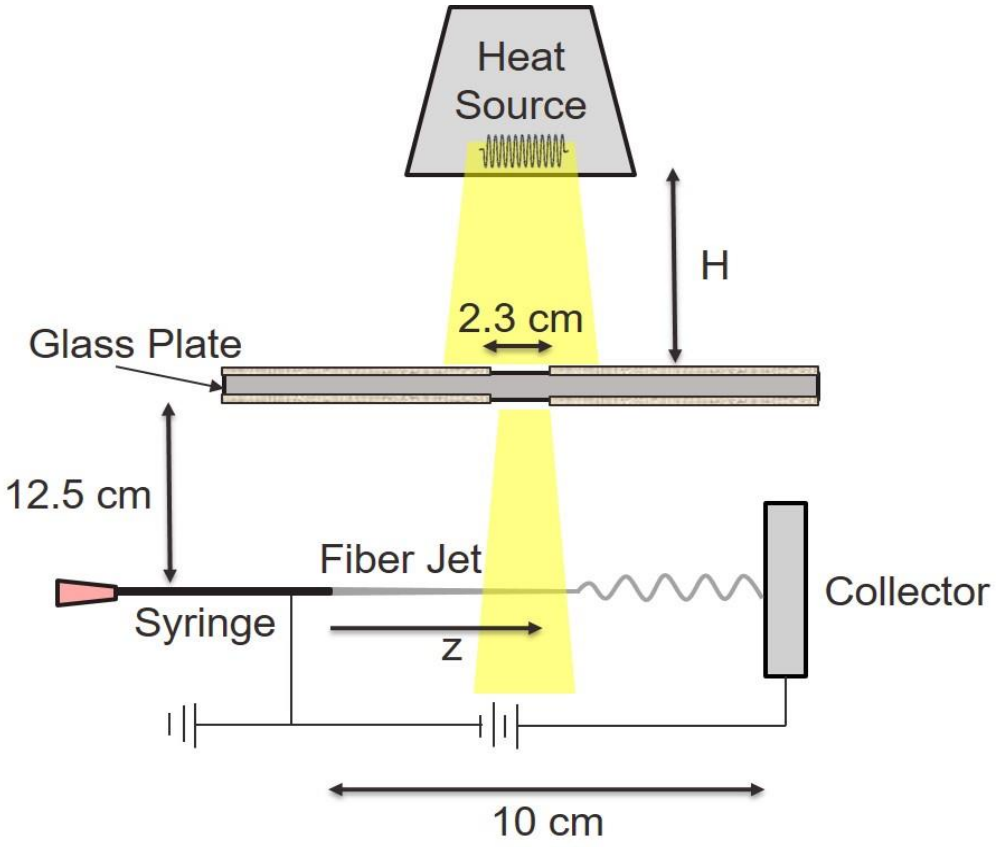

Figure 5: Schematic of our setup for melt electrospinning PCL.

3.2.2. Experimental procedure

Melt electrospinning was performed at room temperature of 20 °C. The syringe was heated using the syringe heater to 100 °C. The ground cable of the power supply was connected to the syringe needle, and the high negative voltage was connected to the collector. The

voltage of the high negative end was -25 kV for all experiments. The distance between the syringe tip and collector was 10 cm. A glass plate with an opening of 2.3 cm x 2.3 cm was placed at a vertical height of 12.5 cm from the plane of the syringe tip, and above that, the heat source was placed at a variable height (H) in order to vary the amount of heat received by the fiber. The heat received by the fiber was assumed to be purely radiative because the surrounding air temperature was affected by a negligible mount.

The feed rate of polymer was set to 44 mL/h. The high voltage power supply was turned on, and as the jet formed, the heat source was turned on, and fiber was collected for 15 seconds. To stop fiber formation and collection, the electric field was turned off, followed by the heat source immediately after. Four samples at each distance (12 cm, 8 cm, and 4 cm) were collected, and later analyzed to get average fiber diameters.

Figure 6: Actual image of a melt electrospun fiber on the collector.

3.2.3. Characterization

An optical microscope (Olympus SZX16) was used to image the collected fibers and measure the fiber diameter. For each sample, 3 to 6 images were taken and 20 to 30 diameter measurements were taken for each image collected. ImageJ was used to analyze and make diameter measurements. A CCD camera (EO USB 2.0 CCD) with a zoom imaging lens (VZM 450 Zoom Imaging Lens), and extender lens (VZM 450 0.5X Extender Lens) was used to image the initial jet formation and to compare with the model predictions.

CHAPTER IV

RESULTS AND DISCUSSION

In this section, we first present our simulations for melt electrospinning of PLA. The model predictions as well as experimental results for melt electrospinning of PCL are then presented separately.

For PLA, our model is used to predict the radius and temperature profile of the polymer jet in presence of the downstream volumetric heat source. We also investigate how the fiber radius is affected by varying the surrounding air temperature, the magnitude of downstream heat, as well as the region in which this heat interacts with the fiber. For all our simulations, we have maintained a constant syringe nozzle temperature of 225 ºC and $\chi = 200$ as the dimensionless spinning distance.

For PCL, we compare our model prediction of the initial jet profile to that obtained experimentally in order to validate our current model, and calibrate some of its parameters. Then, using both, model and experiment, we study how the magnitude of heat influences the fiber radius.

4.1. PLA model predictions

4.1.1. Radius and temperature profile of the polymer jet in presence of downstream heat

Here, we investigate the radius and temperature profile of the polymer jet in the presence of a downstream volumetric heat source.

In Figure 7, the heat source interacts with the fiber from the beginning, i.e., from $z/R_0 = 0$ up to $z/R_0 = 20$. The air temperature is maintained constant at 20 ºC for this case.

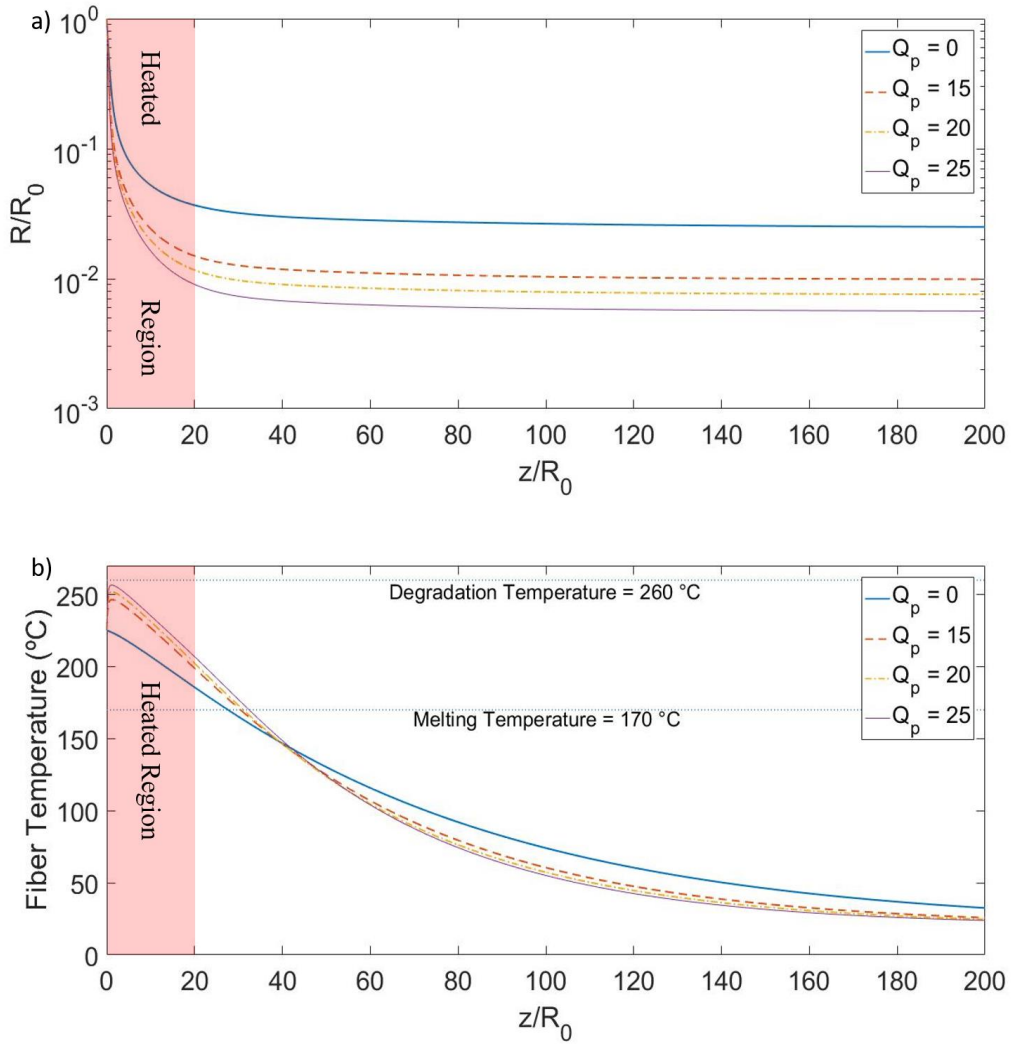

Figure 7: (a) Dimensionless fiber radius profile for the case when no heat is provided ($Q_p = 0$), and when heat is turned on between $0 < z/R_0 < 20$ ($Q_p = 15$, $Q_p = 20$ & $Q_p = 25$) at a constant air temperature of 20 ºC & (b) corresponding fiber temperature profile.

As expected, by providing more heat (or higher Q_p), we can increase the temperature of the jet, thereby keeping the jet in a stretchable state for a longer region. As a result, thinner fibers will form as seen from Figure 7 (a).

In Figure 7 (b), we observe an interesting crossover in the temperature of the polymer jet when it is subjected to different magnitudes of heat, which can be explained as follows. Initially, as expected from the conservation of energy and as shown in Figure 7 (b), a jet subjected to a higher Q_p will have a higher temperature compared to another jet which is subjected to a lower Q_p. The higher temperature of the jet lowers the jet viscosity. Hence, the jet exposed to a higher Q_p would thin down faster causing it to have a higher surface area to volume ratio (which scales inversely with fiber radius). Thus, it would lose heat to the surrounding air via convection more quickly as compared to a jet subjected to a lower Q_p (which is thicker). As a result, the fiber will experience a faster temperature drop, and after a certain point, it would have a lower temperature compared to the other fiber. Therefore, we observe a crossover in the temperature plot when fibers are subject to different Q_p.

Next, we investigate the radius and temperature profile of the polymer jet when we heat the fiber slightly downstream from the syringe nozzle, between $z/R_0 = 80$ and $z/R_0 = 100$. The air temperature is maintained constant at 20 ºC.

In Figure 8, the fiber initially thins down purely under the influence of the electric field. Then, around $z/R_0 = 80$, we notice that for all practical purposes, the initial thinning has stopped. This is indicated in Figure 7 (a) where the plot plateaus out. At this point, we

begin heating the fiber. As seen from the figure, we observe a second thinning regime. This is very interesting, especially from the point of view of our proposed objective, since it hints at the possibility of employing a multi-stage thinning process. Such a process has the potential of thinning down the fiber to a greater extent than what can be achieved via conventional melt electrospinning.

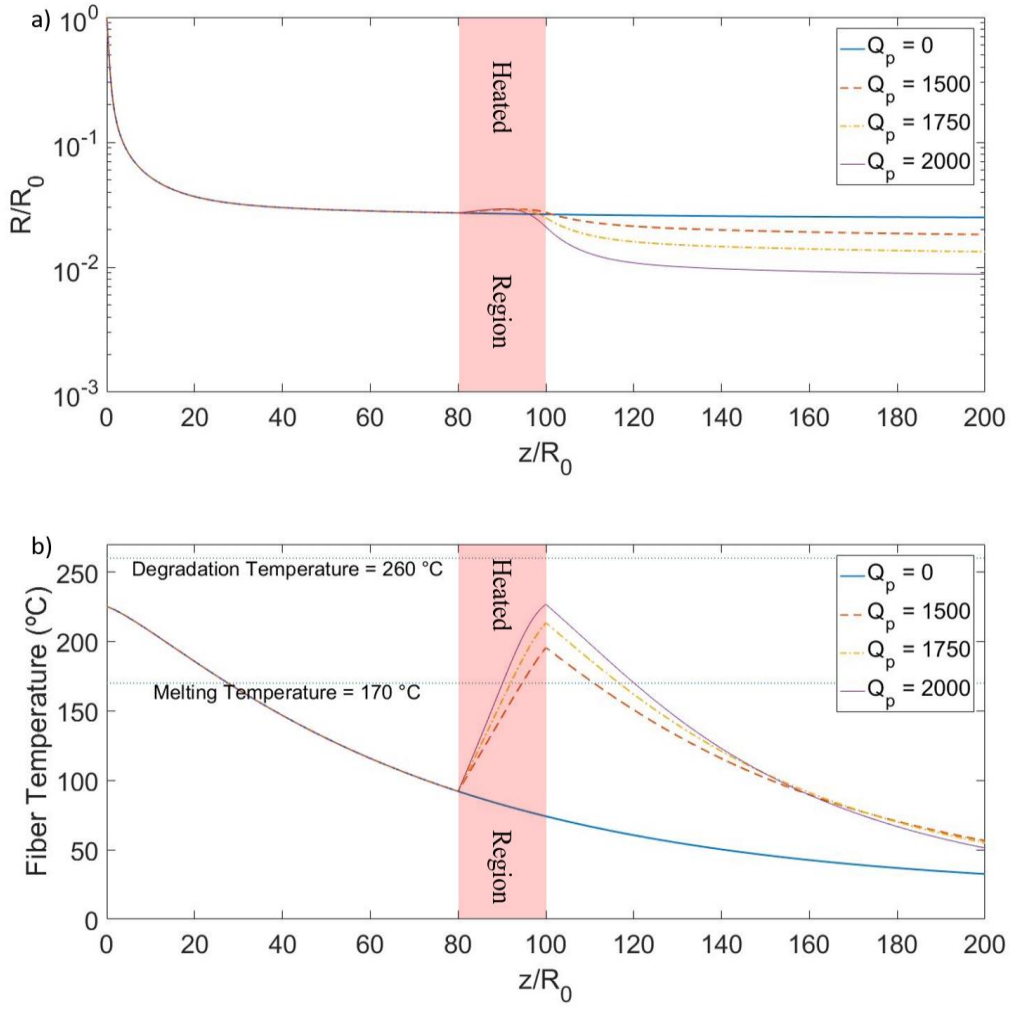

Figure 8: (a) Dimensionless fiber radius profile for the case when no heat is provided (Q_p = 0), and when heat is turned on between 80 < z/R_0 < 100 (Q_p = 1500, Q_p = 1750 & Q_p = 2000) at a constant air temperature of 20 ºC & (b) corresponding fiber temperature profile.

Again, as seen from Figure 8 (b), we observe a crossover in the temperature profiles of the fiber when it is subjected to different Q_p. This can be explained by the same concept as was discussed earlier for the case when the fiber was heated between $0 < z/R_0 < 20$.

Note that as a result of downstream heat provided to the fiber, its temperature increases. In our effort, we try to avoid degradation of the fiber. Therefore, there is a maximum limit of heat that can be provided to the fiber before the fiber can overheat, and thus thermally degrade. This limit is reached when the maximum temperature attained by the fiber is just below its degradation temperature. Due to this, we cannot keep on increasing Q_p because we might cross the degradation temperature of the fiber.

Another important thing to note here is that in order to observe noticeable changes in the fiber diameter, in Figure 7, the dimensionless heat is varied between 0 and 25, but in Figure 8, it is varied between 0 and 2000. This is because of two reasons. First is that the effective heating rate due to Q_p is volumetric, which scales with R^2 (i.e. with jet volume per unit length), while the rate of heat loss is convective which scales with R (i.e. with jet surface area per unit length). Therefore, lowering the jet radius changes the heat balance in favor of convective heat loss. So, when heat is provided in thinner regions of the jet (further downstream), higher volumetric heat (and thus higher Q_p) is required to overcome the convective heat loss. Second reason is that, when the fiber is exposed to volumetric heat in Figure 8 ($80 < z/R_0 < 100$), it is already significantly thin compared to the case in Figure 7 when the fiber is heated between $0 < z/R_0 < 20$.

These simulation results demonstrate the fact that incorporating a downstream heat source can actually bring about a considerable degree of thinning, and is therefore a feasible solution for addressing the drawbacks of melt electrospinning.

4.1.2. Combined effect of surrounding air temperature, magnitude of downstream heat, and region over which it is provided

This section explores how the fiber radius is influenced by the surrounding air temperature, the magnitude of volumetric heat, and the location where this heat is provided. Dimensionless fiber radius is plotted vs. air temperature, which is varied between 20 ºC and 120 ºC. In each plot, different trends are analyzed by varying the amount of volumetric heat provided to the fiber.

We first discuss the case where volumetric heat is turned on between $0 < z/R_0 < 20$, as shown in Figure 9 (a). In order to obtain the same fiber radius, one could either provide a larger Q_p and operate at a lower air temperature or provide a smaller Q_p and operate at a higher air temperature. However, in the limit of higher air temperature, one can encounter the problem of ensuring that the fiber is fully solidified before hitting the target. In contrast, localized downstream heating at a lower air temperature allows for a more precise control over the path of the fiber from melt to solid state prior to hitting the target.

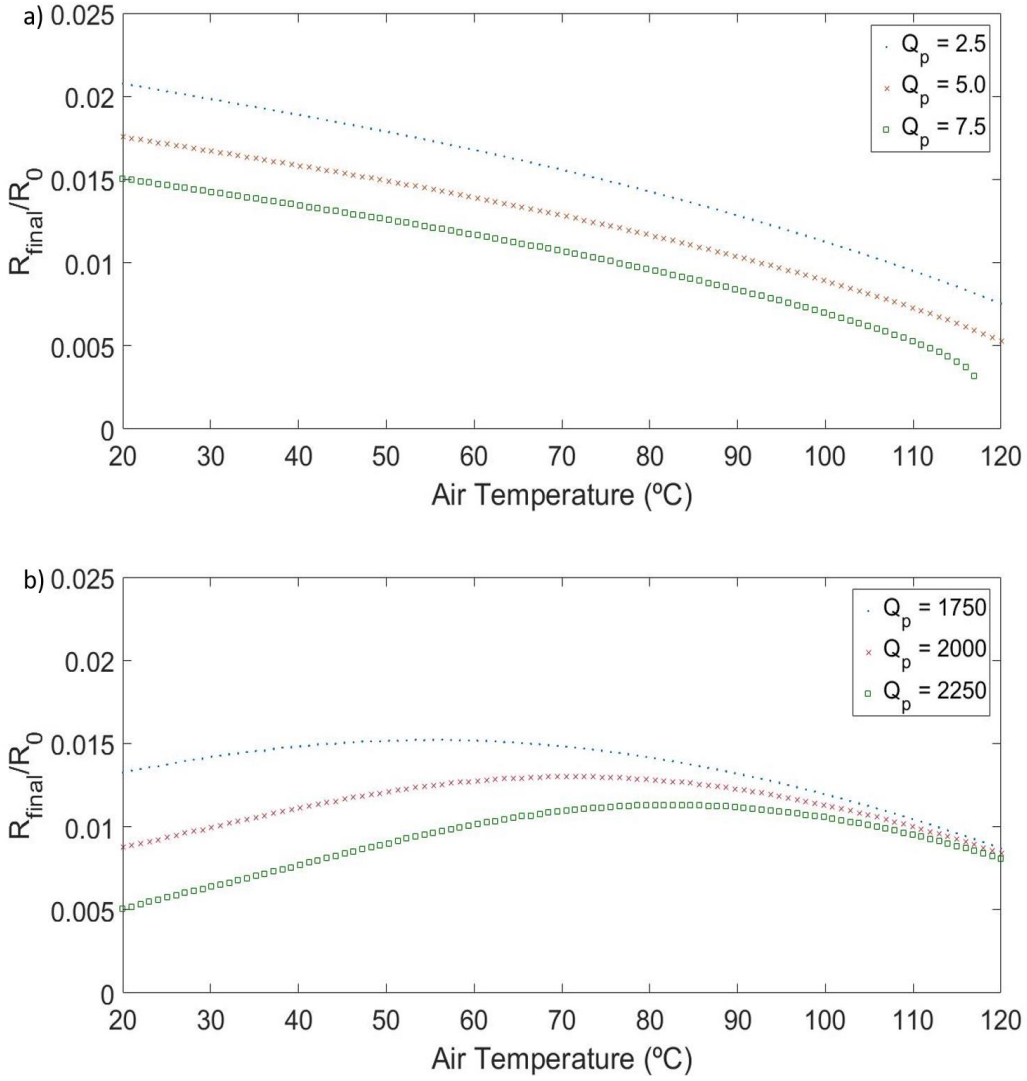

Figure 9: R_{final}/R_0 vs. air temperature for varying values of Q_p for the case when (a) heat is turned on between $0 < z/R_0 < 20$ (Q_p = 2.5, Q_p = 5.0 & Q_p = 7.5) & (b) heat is turned on between $80 < z/R_0 < 100$ (Q_p = 1750, Q_p = 2000 & Q_p = 2250).

Next, we discuss the case wherein volumetric heat is turned on between $80 < z/R_0 < 100$ as depicted in Figure 9 (b). At low air temperature, thinning of the fiber is primarily controlled by the volumetric heat provided to it. In other words, volumetric heat keeps the jet in a melted, and thus stretchable state for a longer region. On the other hand, as air

temperature increases, surface cooling due to convection is slowed down because the driving force for heat loss (difference in fiber temperature and air temperature) is reduced. Thus, by the time the fiber experiences heat (z/R_0 = 80), it is thinner than a corresponding fiber subject to a lower air temperature. Due to this, it absorbs a lower quantity of heat. Therefore, the influence of volumetric heat begins to diminish. Simultaneously, reduced surface cooling due to increased air temperature starts becoming the major factor influencing fiber thinning. At an intermediate air temperature, a trade-off between these effects leads to the occurrence of a maximum in the plot. Subsequently, at high air temperature, the contribution of volumetric heat towards fiber thinning becomes negligible. This is manifested by the convergence of lines representing different Q_p.

Another interesting observation from this figure is that the location of the maximum shifts to the direction of higher air temperature as Q_p increases. This observation is consistent with our reasoning. An increase in the magnitude of volumetric heat provided to the fiber would make it the dominant factor for a longer section of air temperature.

4.1.3. Effect of length over which downstream heat is provided

In this section, we study how the fiber radius is influenced by the length over which volumetric heat is provided to the fiber. We focus on the case when downstream heat is provided from z/R_0 = 80 using Q_p = 1500. Dimensionless radius is plotted against air temperature which is varied between 20 ºC and 120 ºC. Different trends are investigated in this plot by varying the interval for which heat is provided to the fiber.

Increasing the interval over which the fiber experiences the heat is analogous to supplying a greater quantity of volumetric heat (or providing a higher Q_p as studied previously in Section 4.1.2.). The fact that Figure 10 follows a similar trend as Figure 9 (b) reinforces the concept that we described for explaining Figure 9 (b).

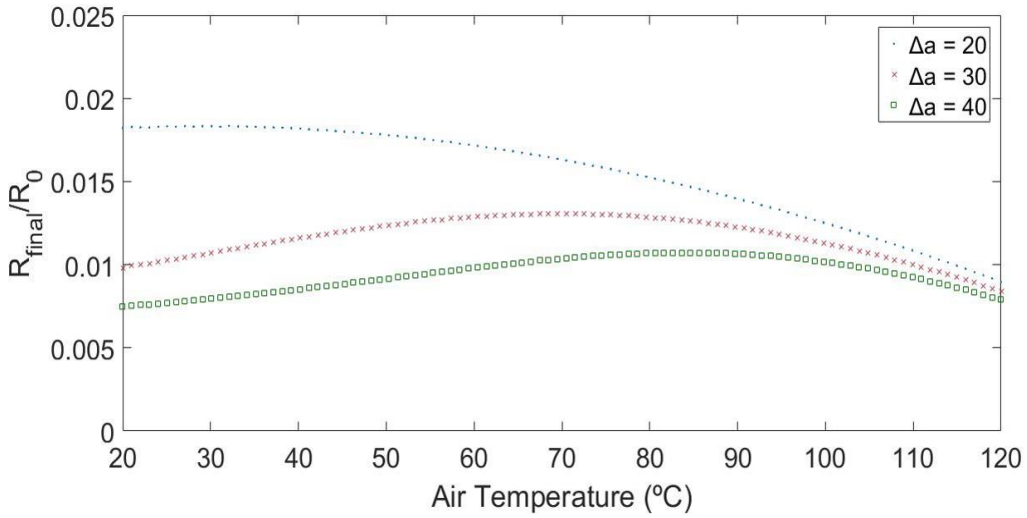

Figure 10: R_{final}/R_0 vs. air temperature for varying values of Δa for the case when Q_p =1500, and when heat is provided from z/R_0 = 80.

4.2. PCL model and experiment

4.2.1. Comparison of the initial jet profile

In order to modify the model to be applicable to PCL, we found material properties of PCL from various sources as shown in Table 3. Moreover, we verified the accuracy of the model by comparing the initial jet profile and final fiber diameter obtained using the model, to that obtained experimentally. An example of the jet profile which was used to measure the jet radius as a function of z/R_0 is shown in Figure 11 (b). The reported radius

of the jet at each value of z/R_0 is an average of several measurements, and the reported errors represent the standard deviation of the measurements. The model slightly underpredicts the jet radius unitl about $z/R_0 = 5$. This is due to the fact that the simulation does not capture the Taylor cone geometery of the electrospinning process, in which there is an inflection point on the jet, which can be seen from the experimental profile in Figure 11 (b).

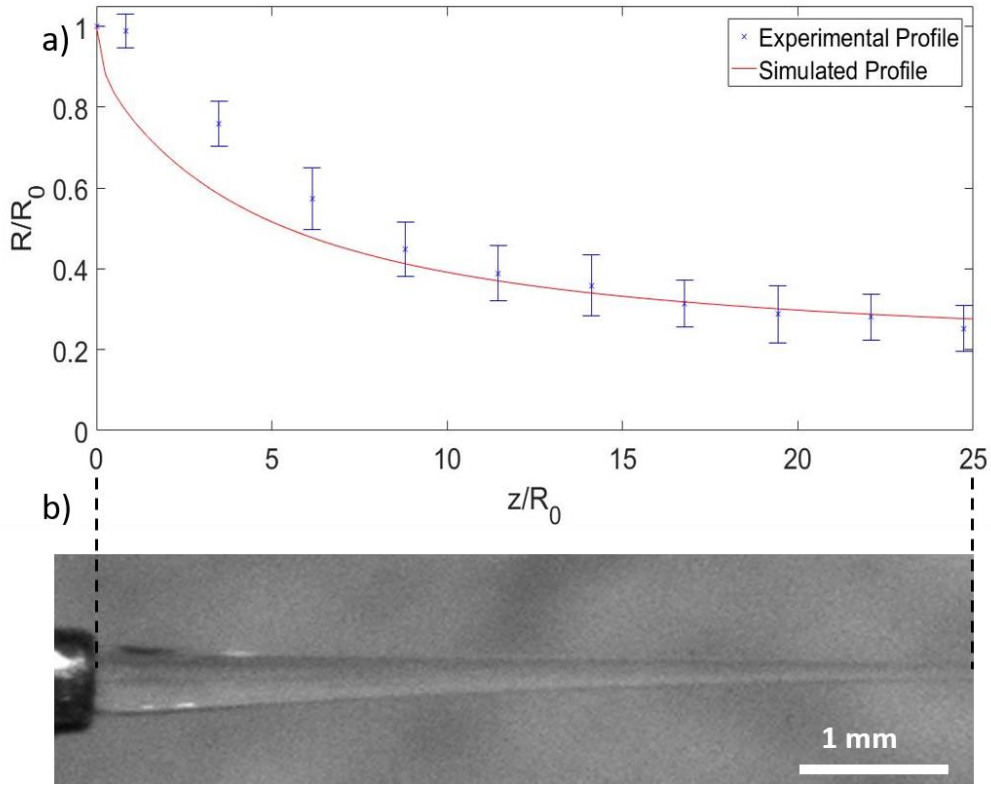

Figure 11: Initial jet profile - (a) comparison between experiment and simulation & (b) CCD image.

4.2.2. Effect of distance of heat source from the fiber

With the experimentally validated model for melt electrospinning, we studied the effect of downstream volumetric heat on the fiber diameter. The magnitude of volumetric heat was controlled by adjusting the distance between the heat lamp and the glass plate. We studied four cases: no radiation (benchmark), and lamp to plate distances of 4 cm, 8 cm, and 12 cm. Optical microscopy was used to measure the melt electrospun fiber diameter. We modeled the lamp as a line heat source such that the heat dissipates radially, similar to Kishore *et al*.[55] Therefore, the quantity of heat absorbed by the fiber varies inversely with distance between the heat source and the polymer jet. After non-dimensionalization and appropriate rearrangement, this modified heat source term was incorporated into the existing energy equation. Using experimental data, we fitted a $Q_{p,characteristic}$ which is characteristic of the heat lamp. Using the line source analysis, we determined the Q_p corresponding to each case.

Figure 12 shows sample optical microscope images of fibers for varying lamp to jet distances. Fiber diameter distributions consistently show a thinner diameter for increasing magnitudes of heat. A similar trend was observed from the model as presented in Figure 13. The experiment shows a 12.1%, 18.7%, and 22.7% decrease in diameter for the cases of lamp at 12 cm, 8 cm, and 4 cm, respectively. The model predicts an 11.3%, 16.2%, and 24.8% decrease in diameter for the respective distances. This shows that the experiment and model are in good agreement with each other.

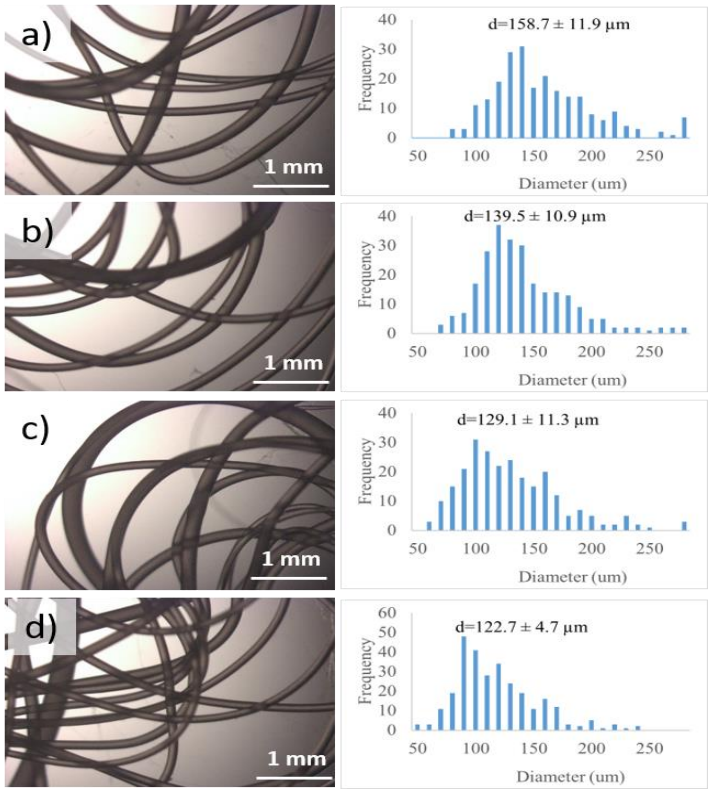

Figure 12: Optical microscope images with (a) no heat, and heat lamp at (b) 12 cm, (c) 8 cm & (d) 4 cm.

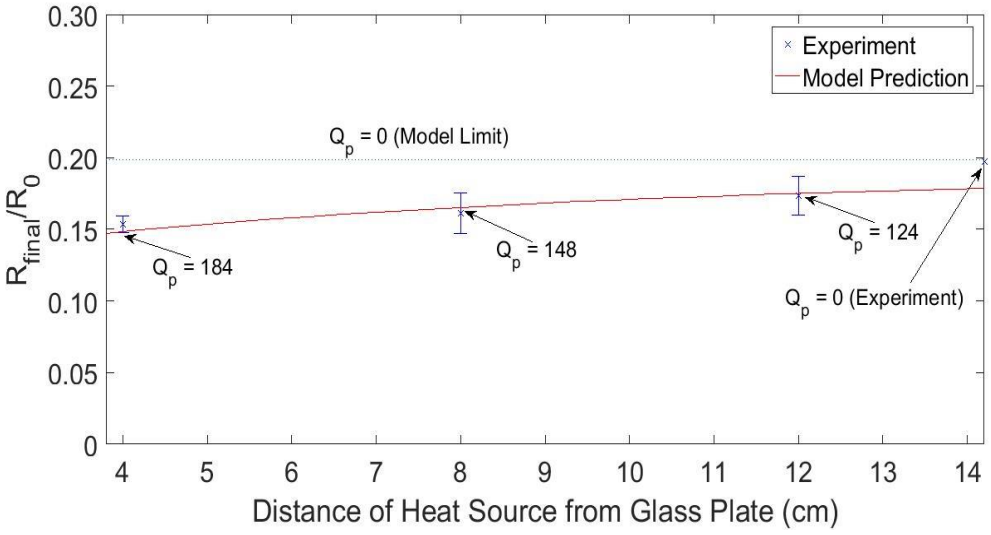

Figure 13: Dimensionless fiber radius vs. distance of heat source from the glass plate.

CHAPTER V

CONCLUSIONS AND FUTURE WORK

We have utilized a model for non-isothermal melt electrospinning with a volumetric heat source in order to demonstrate that downstream heating in the spinning process assists in the thinning of melt electrospun fibers. The model is based on thin filament approximation applied to fully coupled momentum, continuity, charge, and energy equations, along with the non-isothermal Giesekus constitutive model and the electric field equation at steady state.

The simulation results for PLA validate that the concept of downstream heating leads to a decrease in the fiber radius. Therefore, it is a practical solution for addressing the drawbacks of melt electrospinning. In addition, the model has been used to study how the fiber radius is influenced by surrounding air temperature, magnitude of downstream heat, and the region over which this heat is provided to the fiber.

For PCL, the simulated initial jet profile has been quantitatively compared to an experimental image of the stable jet near the syringe nozzle. In addition, the predicted effect of the downstream volumetric heat on the final radius of PCL is compared to the experimentally obtained average fiber radius. The simulated results are in agreement with the experimentally acquired data under difference processing conditions.

Therefore, this study establishes that melt electrospinning coupled with downstream heating, as a method to produce sub-micron fibers, could be useful to industry. Such

techniques are cost-effective, environmentally friendly, and inherently safe. Downstream heating allows for the scalable production of sub-micron fibers which is otherwise very difficult to achieve with melt electrospinning.

However, the results presented for PCL point to moderate reductions of fiber diameter via simple means of downstream heating, such as a heat lamp. More significant reduction in fiber diameter, demands stronger coupling between the heat source and the polymer jet, so that the jet can be maintained in a stretchable state over a longer region. This can be achieved by, for instance, addition of nanoparticle additives to the polymer, which are receptors of electromagnetic radiation. Such a technique would alter the physics of the problem, and would therefore require a modified analytical and experimental approach, as will be the subject of future studies.

REFERENCES

(1) Huang, C.; Soenen, S. J.; Rejman, J.; Lucas, B.; Braeckmans, K.; Demeester, J.; De Smedt, S. C. Stimuli-responsive electrospun fibers and their applications. *Chemical Society Reviews* **2011**, *40*, 2417-2434.

(2) Cavaliere, S.; Subianto, S.; Savych, I.; Jones, D. J.; Rozière, J. Electrospinning: designed architectures for energy conversion and storage devices. *Energy & Environmental Science* **2011**, *4*, 4761-4785.

(3) Long, Y.-Z.; Li, M.-M.; Gu, C.; Wan, M.; Duvail, J.-L.; Liu, Z.; Fan, Z. Recent advances in synthesis, physical properties and applications of conducting polymer nanotubes and nanofibers. *Progress in Polymer Science* **2011**, *36*, 1415-1442.

(4) Wang, N.; Mao, X.; Zhang, S.; Yu, J.; Ding, B.: Electrospun nanofibers for air filtration. *Electrospun Nanofibers for Energy and Environmental Applications*; Springer **2014**; pp 299-323.

(5) Gopal, R.; Kaur, S.; Ma, Z.; Chan, C.; Ramakrishna, S.; Matsuura, T. Electrospun nanofibrous filtration membrane. *Journal of Membrane Science* **2006**, *281*, 581-586.

(6) Pham, Q. P.; Sharma, U.; Mikos, A. G. Electrospinning of polymeric nanofibers for tissue engineering applications: a review. *Tissue engineering* **2006**, *12*, 1197-1211.

(7) Vasita, R.; Katti, D. S. Nanofibers and their applications in tissue engineering. *International Journal of nanomedicine* **2006**, *1*, 15.

(8) Hu, X.; Liu, S.; Zhou, G.; Huang, Y.; Xie, Z.; Jing, X. Electrospinning of polymeric nanofibers for drug delivery applications. *Journal of Controlled Release* **2014**, *185*, 12-21.

(9) Huang, Z.-M.; Zhang, Y.-Z.; Kotaki, M.; Ramakrishna, S. A review on polymer nanofibers by electrospinning and their applications in nanocomposites. *Composites science and technology* **2003**, *63*, 2223-2253.

(10) Yan, H.; Mahanta, N. K.; Majerus, L. J.; Abramson, A. R.; Cakmak, M. Thermal conductivities of electrospun polyimide-mesophase pitch nanofibers and mats. *Polymer Engineering & Science* **2014**, *54*, 977-983.

(11) Shi, X.; Zhou, W.; Ma, D.; Ma, Q.; Bridges, D.; Ma, Y.; Hu, A. Electrospinning of nanofibers and their applications for energy devices. *Journal of Nanomaterials* **2015**, *16*, 122.

(12) Nayak, R.; Padhye, R.; Kyratzis, I. L.; Truong, Y. B.; Arnold, L. Effect of viscosity and electrical conductivity on the morphology and fiber diameter in melt electrospinning of polypropylene. *Textile Research Journal* **2013**, *83*, 606-617.

(13) Zhmayev, E.; Zhou, H.; Joo, Y. L. Modeling of non-isothermal polymer jets in melt electrospinning. *Journal of Non-Newtonian Fluid Mechanics* **2008**, *153*, 95-108.

(14) Ziabicki, A.: *Fundamentals of fibre formation : the science of fibre spinning and drawing*; Wiley: London **1976**; pp xiv.

(15) Reneker, D. H.; Yarin, A. L. Electrospinning jets and polymer nanofibers. *Polymer* **2008**, *49*, 2387-2425.

(16) Thomas, S. W.; Pais, Y.; Alcantar, N. A. Electrospun cactus mucilage nanofibers. Google Patents **2013**.

(17) Kurečič, M.; Smole, M. S. Electrospinning: Nanofibre Production Method. *Tekstilec* **2013**, *56*.

(18) Karakaş, H. Electrospinning of Nanofibers and their Applications.

(19) Carroll, C. P.; Joo, Y. L. Electrospinning of viscoelastic Boger fluids: Modeling and experiments. *Physics of Fluids* **2006**, *18*, 053102.

(20) Zhou, H.: Electrospun fibers from both solution and melt: Processing, structure and property. The American Chemical Society **2006**.

(21) Haider, A.; Haider, S.; Kang, I.-K. A comprehensive review summarizing the effect of electrospinning parameters and potential applications of nanofibers in biomedical and biotechnology. *Arabian Journal of Chemistry* **2015**.

(22) Weitz, R.; Harnau, L.; Rauschenbach, S.; Burghard, M.; Kern, K. Polymer nanofibers via nozzle-free centrifugal spinning. *Nano letters* **2008**, *8*, 1187-1191.

(23) Edmondson, D.; Cooper, A.; Jana, S.; Wood, D.; Zhang, M. Centrifugal electrospinning of highly aligned polymer nanofibers over a large area. *Journal of Materials Chemistry* **2012**, *22*, 18646-18652.

(24) Bhardwaj, N.; Kundu, S. C. Electrospinning: a fascinating fiber fabrication technique. *Biotechnology advances* **2010**, *28*, 325-347.

(25) Agarwal, S.; Wendorff, J. H.; Greiner, A. Progress in the field of electrospinning for tissue engineering applications. *Advanced Materials* **2009**, *21*, 3343-3351.

(26) Huang, L.; Manickam, S. S.; McCutcheon, J. R. Increasing strength of electrospun nanofiber membranes for water filtration using solvent vapor. *Journal of membrane science* **2013**, *436*, 213-220.

(27) Góra, A.; Sahay, R.; Thavasi, V.; Ramakrishna, S. Melt-electrospun fibers for advances in biomedical engineering, clean energy, filtration, and separation. *Polymer Reviews* **2011**, *51*, 265-287.

(28) Zhang, L.-H.; Duan, X.-P.; Yan, X.; Yu, M.; Ning, X.; Zhao, Y.; Long, Y.-Z. Recent advances in melt electrospinning. *RSC Advances* **2016**, *6*, 53400-53414.

(29) Zhou, H.; Green, T. B.; Joo, Y. L. The thermal effects on electrospinning of polylactic acid melts. *Polymer* **2006**, *47*, 7497-7505.

(30) Lyons, J.; Li, C.; Ko, F. Melt-electrospinning part I: processing parameters and geometric properties. *Polymer* **2004**, *45*, 7597-7603.

(31) Qin, C.-C.; Duan, X.-P.; Wang, L.; Zhang, L.-H.; Yu, M.; Dong, R.-H.; Yan, X.; He, H.-W.; Long, Y.-Z. Melt electrospinning of poly (lactic acid) and polycaprolactone microfibers by using a hand-operated Wimshurst generator. *Nanoscale* **2015**, *7*, 16611-16615.

(32) Detta, N.; Brown, T. D.; Edin, F. K.; Albrecht, K.; Chiellini, F.; Chiellini, E.; Dalton, P. D.; Hutmacher, D. W. Melt electrospinning of polycaprolactone and its blends with poly (ethylene glycol). *Polymer international* **2010**, *59*, 1558-1562.

(33) Deitzel, J. M.; BeckTan, N. C.; Kleinmeyer, J. D.; Rehrmann, J.; Tevault, D. *Generation of Polymer Nanofibers Through Electrospinning* **1999**.

(34) Reneker, D. H.; Chun, I. Nanometer diameter fibers of polymer, produced by electrospinning. *Nanotechnology* **1996**, *7*, 216.

(35) Sukigara, S.; Gandhi, M.; Ayutsede, J.; Micklus, M.; Ko, F. Regeneration of Bombyx mori silk by electrospinning part 1: processing parameters and geometric properties. *Polymer* **2003**, *44*, 5721-5727.

(36) Wang, Q.; Curtis, C. K.; Thoppey, N. M.; Bochinski, J. R.; Gorga, R. E.; Clarke, L. I. Unconfined, melt edge electrospinning from multiple, spontaneous, self-organized polymer jets. *Materials Research Express* **2014**, *1*, 045304.

(37) Menéndez, J.; Arenillas, A.; Fidalgo, B.; Fernández, Y.; Zubizarreta, L.; Calvo, E. G.; Bermúdez, J. M. Microwave heating processes involving carbon materials. *Fuel Processing Technology* **2010**, *91*, 1-8.

(38) Schnabel, W.: *Polymers and Electromagnetic Radiation: Fundamentals and Practical Applications*; John Wiley & Sons **2014**.

(39) Mohr, R.; Kratz, K.; Weigel, T.; Lucka-Gabor, M.; Moneke, M.; Lendlein, A. Initiation of shape-memory effect by inductive heating of magnetic nanoparticles in thermoplastic polymers. *Proceedings of the National Academy of Sciences of the United States of America* **2006**, *103*, 3540-3545.

(40) Reneker, D. H.; Yarin, A. L.; Fong, H.; Koombhongse, S. Bending instability of electrically charged liquid jets of polymer solutions in electrospinning. *Journal of Applied physics* **2000**, *87*, 4531-4547.

(41) Yarin, A. L.; Koombhongse, S.; Reneker, D. H. Bending instability in electrospinning of nanofibers. *Journal of Applied Physics* **2001**, *89*, 3018-3026.

(42) Shin, Y.; Hohman, M.; Brenner, M.; Rutledge, G. Experimental characterization of electrospinning: the electrically forced jet and instabilities. *Polymer* **2001**, *42*, 09955-09967.

(43) Hohman, M. M.; Shin, M.; Rutledge, G.; Brenner, M. P. Electrospinning and electrically forced jets part I: stability theory. *Physics of fluids* **2001**, *13*, 2201-2220.

(44) Hohman, M. M.; Shin, M.; Rutledge, G.; Brenner, M. P. Electrospinning and electrically forced jets part II: applications. *Physics of fluids* **2001**, *13*, 2221-2236.

(45) Spivak, A.; Dzenis, Y. A. Asymptotic decay of radius of a weakly conductive viscous jet in an external electric field. *Applied Physics Letters* **1998**, *73*, 3067-3069.

(46) Feng, J. The stretching of an electrified non-Newtonian jet: A model for electrospinning. *Physics of Fluids* **2002**, *14*, 3912-3926.

(47) Feng, J. Stretching of a straight electrically charged viscoelastic jet. *Journal of Non-Newtonian Fluid Mechanics* **2003**, *116*, 55-70.

(48) Matsuo, T.; Kase, S. Studies on melt spinning part VII: temperature profile within the filament. *Journal of Applied Polymer Science* **1976**, *20*, 367-376.

(49) Joo, Y.; Sun, J.; Smith, M.; Armstrong, R.; Brown, R.; Ross, R. Two-dimensional numerical analysis of non-isothermal melt spinning with and without phase transition. *Journal of Non-Newtonian Fluid Mechanics* **2002**, *102*, 37-70.

(50) Kirichenko, V.; Suprun, N.; Petrianovsokolov, I. Form of a free stationary fluid stream in a strong uniform electric field. *Doklady Akademii Nauk* **1987**, *295*, 553-555.

(51) Genina, N.; Holländer, J.; Jukarainen, H.; Mäkilä, E.; Salonen, J.; Sandler, N. Ethylene vinyl acetate (EVA) as a new drug carrier for 3D printed medical drug delivery devices. *European Journal of Pharmaceutical Sciences* **2016**, *90*, 53-63.

(52) Sunthar, P.: Polymer rheology. In *Rheology of Complex Fluids*; Springer, **2010**; pp 171-191.

(53) Kalenov, D.; Meriakri, V.; Parkhomenko, M.; Zhou, S.; D'Amore, A.; Grassia, L.; Acierno, D. Modeling the Strength Degradation and Fatigue of Carbon Fiber Reinforced Composites. *AIP Conference* **2012**.

(54) Baker, S. R.; Banerjee, S.; Bonin, K.; Guthold, M. Determining the mechanical properties of electrospun poly-ε-caprolactone (PCL) nanofibers using AFM and a novel fiber anchoring technique. *Materials Science and Engineering: C* **2016**, *59*, 203-212.

(55) Kishore, V.; Ajinjeru, C.; Nycz, A.; Post, B.; Lindahl, J.; Kunc, V.; Duty, C. Infrared preheating to improve interlayer strength of big area additive manufacturing (BAAM) components. *Additive Manufacturing* **2017**, *14*, 7-12.

APPENDIX A

MODEL FORMULATION

The model has been formulated as an initial value problem of a set of five coupled first order ordinary differential equations.

The first equation in our system is as follows:

$$R' = \hat{R} \tag{34}$$

From equation (15) we get the following relations:

$$v = \frac{1}{R^2} \tag{35}$$

$$v' = \frac{-2R'}{R^3} \tag{36}$$

From equations (23), (24) and (36) we get the following relation:

$$\tau_{zz} - \tau_{rr} = \tau_{p,zz} - \tau_{p,rr} + -\frac{6\beta f(\theta)R'}{R^3} \tag{37}$$

On substituting equations (35), (36) and (37) into equation (21) and subsequently rearranging it, we get:

$$\theta' = \frac{-2NaR'}{PeR}\left(\tau_{p,zz} - \tau_{p,rr} - \frac{6\beta f(\theta)R'}{R^3}\right) - \frac{2Bi_L(\theta-\theta_\infty)R}{Pe} + \frac{Q_p R^2}{Pe} \tag{38}$$

On substituting equations (35) and (36) into equation (25) and subsequently rearranging it, we get:

$$\tau_{p,zz}{}' = \left(\frac{R^2}{f(\theta)}\right)\left(\frac{(\theta+\Gamma)}{De\Gamma}\right)\left[\frac{-4(1-\beta)f(\theta)R'}{R^3} - \tau_{p,rr} - \frac{De\Gamma}{(\theta+\Gamma)}\left(\frac{\alpha\tau_{p,zz}{}^2}{(1-\beta)} + \frac{4\tau_{p,zz}f(\theta)R'}{R^3} - \left(\frac{f(\theta)}{R^2}\right)\frac{\tau_{p,zz}\theta'}{(\theta+\Gamma)}\right)\right] \quad (39)$$

On substituting equations (35) and (36) into equation (26) and subsequently rearranging it, we get:

$$\tau_{p,rr}{}' = \left(\frac{R^2}{f(\theta)}\right)\left(\frac{(\theta+\Gamma)}{De\Gamma}\right)\left[\frac{2(1-\beta)f(\theta)R'}{R^3} - \tau_{p,zz} - \frac{De\Gamma}{(\theta+\Gamma)}\left(\frac{\alpha\tau_{p,zz}{}^2}{(1-\beta)} - \frac{2\tau_{p,rr}f(\theta)R'}{R^3}\right)\right] \quad (40)$$

On substituting equations (35), (36) and (37) into equation (16) and subsequently rearranging it, we get:

$$\hat{R}' = R'' = \frac{R^3}{\mathbf{6}\beta\boldsymbol{f}(\theta)}\left[\frac{2ReR'}{R^5} + Bo + \frac{2R'}{R}\left(\tau_{p,zz} - \tau_{p,rr} + -\frac{6\beta f(\theta)R'}{R^3}\right) + \left(\tau_{p,zz}{}' - \tau_{p,rr}{}' + + \frac{18\beta f(\theta)R'^2}{R^4}\right) + \frac{R'}{CaR^2} + Fe\left(\sigma\sigma' + \beta_E E_t E_t{}' + \frac{2\sigma E_t}{R}\right)\right] \quad (41)$$

Equations (34), (38), (39), (40) and (41) are set up in MATLAB to solve for *R, θ, $\tau_{p,zz}$, $\tau_{p,rr}$* and *R'*, respectively.

APPENDIX B

MATLAB CODE

Function describing our system of coupled ODEs

```
%Function containing the set of coupled ODEs
function dydx = NonIsothermalElectrospinningODEIVP(x,y,Par)
dydx = y*0; %Initialize
dydx(1) = y(5); %Equation (34)
f = exp((Par.H/(Par.R*Par.deltaT))*((1/(y(2) + Par.gamma)) -
(1/Par.gamma))); %Equation (27)
Qp = (Par.Qpm*(heaviside(x - Par.a) - heaviside(x - Par.b)));
%Dimensionless heat source parameter for PLA
dydx(2) = ((-2*Par.Na*y(5))/(Par.Pe*y(1)))*(y(3) - y(4) -
((6*Par.beta)/y(1)^3)*f*y(5)) -
((2*(Par.Bi*((1/y(1)^4)^(1/3))*(((1 + (8*Par.vair*y(1)^2)^2)/(1
+ (8*Par.vair)^2))^(1/6)))*y(1))/Par.Pe)*(y(2) -
Par.thetainfinity) + (Qp/Par.Pe)*y(1)^2; %Equation (38)
dydx(3) = ((y(1)^2/f)*((y(2) +
Par.gamma)/(Par.De*Par.gamma)))*(((-4/y(1)^3)*(1 -
Par.beta)*f*y(5)) - y(3) - ((Par.De*Par.gamma)/(y(2) +
Par.gamma))*(((Par.alpha*y(3)^2)/(1 - Par.beta)) +
((4/y(1)^3)*(y(3)*f*y(5))) - ((1/y(1)^2)*f*(y(3)*dydx(2)/(y(2) +
Par.gamma))))); % Equation (39)
dydx(4) = ((y(1)^2/f)*((y(2) +
Par.gamma)/(Par.De*Par.gamma)))*(((2/y(1)^3)*(1 -
Par.beta)*f*y(5)) - y(4) - (((Par.De*Par.gamma)/(y(2) +
Par.gamma))*(((Par.alpha*y(4)^2)/(1 - Par.beta)) + ((-
2/y(1)^3)*(y(4)*f*y(5)))))); %Equation (40)
Et = 1/((1 + 2*x - x^2/Par.chi)*((1 + y(5)^2)^0.5)); %Equation
(19)
```

```
dEt = (-2 + (2*x/Par.chi))/(((1 + 2*x - x^2/Par.chi)^2)*((1 +
y(5)^2)^0.5)); %Equation (20)
sigma = y(1) - (1/Par.Pec)*y(1)^3*Et; %Equation (17)
dsigma = y(5) - (1/Par.Pec)*((3*y(1)^2*y(5)*Et) + (y(1)^3*dEt));
%Equation (18)
df = exp((Par.H/(Par.R*Par.deltaT))*((1/(y(2) + Par.gamma)) -
(1/Par.gamma)))*(Par.H/(Par.R*Par.deltaT))*(-1/((y(2) +
Par.gamma)^2))*dydx(2); %Equation (28)
dydx(5) = (y(1)^3/(6*Par.beta))*(1/f)*(((2*Par.Re*y(5))/y(1)^5)
+ Par.Bo + ((2*y(5)/y(1))*(y(3) - y(4) -
(6/y(1)^3)*(f*Par.beta*y(5)))) + (dydx(3) - dydx(4) +
((18/y(1)^4)*Par.beta*f*y(5)^2) -
(((6*Par.beta)/y(1)^3)*df*y(5))) + (y(5)/(Par.Ca*y(1)^2)) +
(Par.Fe*((sigma*dsigma) + (Par.betaE*Et*dEt) +
(2*sigma*Et)/(y(1))))); %Equation (41)
end
```

Function describing our initial conditions

```
%Function containing the initial conditions
function [R,theta,tpzz,tprr,dR] =
NonIsothermalElectrospinningIC(Par)
dRguess = -1;
R = 1; %Equation (32)
theta = 0; %Equation (31)
dR = fsolve(@problemdR,dRguess,[],Par); %Obtained by solving
equation (33)
tpzz = 2*(1 - Par.beta)*(-2*dR); %Equation (29)
tprr = -(1 - Par.beta)*(-2*dR); %Equation (30)
end

function fdR = problemdR(dR,Par)
```

```
fdR = 6*dR^2 + ((1/Par.Ca) + Par.Fe)*dR + ((2*Par.Fe)/((1 +
dR^2)^(0.5)))*(1 - (Par.betaE/((1 + dR^2)^(0.5)))); %Equation
(33)
end
```

Sample main function

This function is used for generating the radius and temperature profile for PLA corresponding to the case where $Q_p = 0$ (heat provided between $0 < z/R_0 < 20$).

```
%Main function
%Heat provided between 0 < z/R0 < 20
%Qp = 0
function [] = NonIsothermalElectrospinningODEIVPResult()
% PLA
Par.H = (9060*8.314); %Activation energy of flow
Par.R = 8.314; %Universal gas constant
Par.Tnozzle = (225 + 273); %Nozzle temperature
Par.deltaT = (Par.Tnozzle^2)/(Par.H/Par.R); %Temperature change
necessary to substantially alter the rheological properties of
the polymer melt
Par.gamma = Par.Tnozzle/Par.deltaT; %Temperature factor
Par.vair = 0; %Air velocity
Par.Na = 2.532*10^(-5); %Nahme-Griffith number
Par.Pe = 4.770; %Peclet number for thermal conductivity
Par.beta = 0.001; %Viscosity ratio
Par.Bi = 0.0103; %Biot number
Par.De = 0.0270; %Deborah number
Par.alpha = 0.015; %Mobility factor
Par.Pec = 0.294; %Peclet number for electrical conductivity
Par.chi = 200; %Ratio of length of experimental setup to intial
radius of the polymer melt
```

```
Par.Re = 2.564*10^(-6); %Reynolds number for flow
Par.Bo = 0; %Bond number (It is equal to 0 since the flow is not
influenced by gravity)
Par.Ca = 4.264; %Capillary number
Par.Fe = 3.324; %Electrostatic force parameter
Par.betaE = 2.1; %Dielectric constant ratio
Par.Qpm = 0; %Magnitude of heat source
Par.a = 0; %Start of heat
Par.b = Par.a + 20; %End of heat
Par.Tair = (20 + 273); %Surrounding air temperature
Par.thetainfinity = (Par.Tair - Par.Tnozzle)/Par.deltaT;
x = linspace(0,Par.chi,1000);
[R,theta,tpzz,tprr,dR] = NonIsothermalElectrospinningIC(Par);
initial = [R theta tpzz tprr dR]; %Initial conditions
M = [1 0 0 0 0;0 1 0 0 0;0 0 1 0 0;0 0 0 1 0;0 0 0 0 1];
options = odeset('AbsTol',10^(-10),'Mass',M);
format longeng;
[x,Q] =
ode23s(@NonIsothermalElectrospinningODEIVP,x,initial,options,Par
); %Solving the system of ODEs using an implicit time stepper
%Radius profile
semilogy(x,Q(:,1),'-','LineWidth',0.7);
xlabel('z/R_0');
ylabel('R/R_0');
legend('Q_p = 0');
figure;
%Temperature profile
JetTemperature = (Par.Tnozzle - 273) + Par.deltaT*Q(:,2);
plot(x,JetTemperature,'-','LineWidth',0.7);
xlabel('z/R_0');
ylabel('Fiber Temperature (°C)');
legend('Q_p = 0');
end
```